Excitation of phonons in medium-energy electron diffraction

M. A. Vicente Alvarez, H. Ascolani,* and G. Zampieri
Centro Atómico Bariloche and Instituto Balseiro, Comisión Nacional de Energía Atómica, 8400-Bariloche, Argentina
(Received 20 October 1995)

The ''elastic'' backscattering of electrons from crystalline surfaces presents two regimes: a low-energy regime, in which the characteristic low-energy electron diffraction (LEED) pattern is observed, and a medium-energy regime, in which the diffraction pattern is similar to those observed in x-ray photoemission diffraction (XPD) and Auger electron diffraction (AED) experiments. We present a model for the electron scattering which, including the vibrational degrees of freedom of the crystal, contains both regimes and explains the passage from one regime to the other. Our model is based on a separation of the electron and atomic motions (*adiabatic* approximation) and on a cluster-type formulation of the multiple scattering of the electron. The inelastic scattering events (excitation and/or absorption of phonons) are treated as coherent processes and no break of the phase relation between the incident and the exit paths of the electron is assumed. The LEED and the medium-energy electron diffraction regimes appear naturally in this model as the limit cases of completely elastic scattering and of inelastic scattering with excitation and/or absorption of multiple phonons. Intensity patterns calculated with this model are in very good agreement with recent experiments of electron scattering on Cu(001) at low and medium energies. We show that there is a correspondence between the type of intensity pattern and the mean number of phonons excited and/or absorbed during the scattering: a LEED-like pattern is observed when this mean number is less than 2, LEED-like and XPD/AED-like features coexist when this number is 3–4, and a XPD/AED-like pattern is observed when this number is greater than 5–6.

I. INTRODUCTION

X-ray photoelectron diffraction (XPD) and Auger electron diffraction (AED) have developed during the last years as powerful tools for surface crystallography. In contrast to low-energy electron diffraction (LEED), these diffraction techniques do not require long-range order, are element specific, and are related directly to the real lattice.

The physics underlying these diffraction techniques is by now well understood.[1–3] There exists a well tested theoretical framework that allows one to interpret the experimental data and to determine structural parameters with high accuracy. The basic idea is that the wave representing the electron emitted from an atomic site interferes with the secondary waves produced by the scattering in the neighboring atoms, giving rise to a diffraction pattern. At electron energies above 500 eV these diffraction patterns are characterized by maxima of intensity along the main internuclear directions, which are caused by a special type of interference called *forward focusing*.[2]

The diffraction patterns of medium-energy elastically backscattered electrons are in general very similar to those measured in XPD and AED at similar energies. The first observations were performed in the 1970s,[4–7] but its use as a structural tool comparable to XPD and AED began only recently.[8–13] In contrast to XPD and AED, medium-energy electron diffraction (MEED) is not element specific, but is very fast, because the large signal-to-background ratio of the elastic peak allows diffraction data to be obtained in a short period of time. This high collection speed may be very important when studying time-dependent phenomena, such as interdiffusion or surface segregation, or when collection of a large body of data is needed, as, for example, to make electron holographies.[11]

Unlike the case of XPD and AED, the physics of MEED is not yet fully understood. It is generally assumed that the electron undergoes an inelastic collision at a lattice site and that thereafter it evolves as having been emitted from that site. The first experiments were interpreted in terms of Kikuchi diffraction (electron channeling between planes of atoms),[5,7] but it was then realized that diffraction of a wave emanating from an atomic site, as considered in XPD and AED, was a better starting point for a quantitative description of the experiments. So far the experimental intensities have been reproduced using calculation schemes developed for diffuse LEED,[9] for XPD/AED,[8,10] and this latter modified to account for the diffraction of the incident beam.[8,13] A common aspect of all these models is the unjustified assumption of a break in the phase relation between the incident and exit beams. The whole process is broken artificially into two parts: the incident and the exit paths, which are then treated independently. This procedure renders the problem tractable with the XPD/AED machinery, but eludes the central question of why the scattering of the electron by the surface atoms behaves as the emission from a single atomic site. Put in other words, the question is: what makes the LEED-like intensity pattern at low energies turn into XPD/AED-like at medium energies?

This paper is intended to address this problem. We present a model for the electron scattering from crystalline surfaces which, including all the vibrational degrees of freedom of the crystal, contains both the LEED-like regime at low electron energies and the XPD/AED-like regime at medium energies. The passage from one regime to the other is explained in terms of the excitation and/or absorption of multiple phonons. The model is derived from first principles and has no *ad hoc* assumptions; it combines the standard theory of the inelastic scattering of neutrons by bulk crystals[14] with a

cluster-type formulation of the multiple scattering of the electron.[15] This work follows a previous publication by the authors in which the vibrational degrees of freedom of the crystal were included only as a "rigid" thermal disorder.[16] Our purpose in the present paper is twofold: (i) to put LEED and MEED on a common conceptual framework, and (ii) to investigate the nature of the transition from the LEED-like intensity pattern at low electron energies to a XPD/AED-like intensity pattern at medium energies.

The paper is organized as follows: in Sec. II we present the model; in Sec. III we compare the results of a calculation based on this model with the measured intensities; in Sec. IV we analyze the interplay of the different contributions to the total intensity and the nature of the transition from one regime to the other; finally, in Sec. V we summarize our main conclusions.

II. THEORY

A. Scattering of electrons by a vibrating lattice

We shall consider the scattering of an electron by a semi-infinite crystal. We shall assume that the only degrees of freedom of the crystal are those associated with the atomic vibrations and, therefore, that the total Hamiltonian can be written as

$$H=H_{\rm ph}+H_e+U(\vec{r},\{\vec{R}\}), \tag{1}$$

where $H_{\rm ph}$ is the Hamiltonian that describes the atomic vibrations, $H_e=\vec{p}^2/2m$ is the Hamiltonian of the free electron, and $U(\vec{r},\{\vec{R}\})$ is the interaction potential between the incident electron and the crystal, with $\vec{r}$ and $\{\vec{R}\}$ denoting the electron and the atomic positions, respectively.

The electron transition probability per unit time from the state $|\vec{k}_i\rangle$, with energy $\epsilon_i=\hbar^2 k_i^2/2m$, to the state $|\vec{k}_f\rangle$, with energy $\epsilon_f=\epsilon_i+\hbar\omega$, is

$$\mathscr{R}=\frac{2\pi}{\hbar}\sum_{|f\rangle}\sum_{|i\rangle}|\langle f|\langle\vec{k}_f|\tau(\epsilon_i+\Omega_i)|\vec{k}_i\rangle|i\rangle|^2 \times\frac{e^{-\Omega_i/k_BT}}{Z}\delta(\Omega_f+\hbar\omega-\Omega_i), \tag{2}$$

where $|i\rangle$ and $|f\rangle$ denote the initial and final states of the lattice, with energies Ω_i and Ω_f, respectively, τ is the transition operator, which can be written in terms of the Green operator G_0 of the nonperturbed Hamiltonian $H_{\rm ph}+H_e$ as

$$\tau(E)=U(\vec{r},\{\vec{R}\})+U(\vec{r},\{\vec{R}\})G_0(E)U(\vec{r},\{\vec{R}\})+\cdots \tag{3}$$

and where we have summed over all the final states of the lattice and over all the initial states populated at temperature T (Z is the partition function of the vibrating lattice).

The quantity measured in an experiment, the cross section $d^2\sigma/d\Omega d\epsilon$, is related to the transition rate $\mathscr{R}$ through

$$\frac{d^2\sigma}{d\Omega d\epsilon}=V^2\frac{m^2}{(2\pi\hbar)^3}\frac{k_f}{k_{iz}}\mathscr{R}, \tag{4}$$

where V is the quantization volume and k_{iz} is the component of $\vec{k}_i$ normal to the surface.

Using in Eq. (2) the integral representation of the δ function one can eliminate the sum over the final states of the lattice and write $\mathscr{R}$ as[14,17]

$$\mathscr{R}=\frac{1}{\hbar^2}\int_{-\infty}^{\infty}dt\ e^{i\omega t}\langle\langle\ \langle\vec{k}_f|\tau(\epsilon_i+\Omega_i)|\vec{k}_i\rangle^* \times\langle\vec{k}_f|\tau(\epsilon_i+\Omega_i;t)|\vec{k}_i\rangle\ \rangle\rangle, \tag{5}$$

where $\tau(\epsilon_i+\Omega_i;t)$ is the time-dependent transition operator in the interaction picture:

$$\tau(\epsilon_i+\Omega_i;t)=e^{iH_{\rm ph}t/\hbar}\tau(\epsilon_i+\Omega_i)e^{-iH_{\rm ph}t/\hbar}$$

and where the symbol $\langle\langle\ \rangle\rangle$ indicates the "thermal average" of the argument over the initial states of the lattice:

$$\langle\langle O\rangle\rangle=\sum_{|i\rangle}\langle i|O(\{\vec{R}\})|i\rangle\frac{e^{-\Omega_i/k_BT}}{Z}.$$

To evaluate the thermal average in the integrand of Eq. (5) we will make the following assumptions: (i) *Adiabatic* approximation. We will neglect the phonon energies which are 10^4-10^5 times smaller than the electron energies; then k_f becomes equal to k_i, G_0 becomes the free-electron Green operator g_0:

$$G_0(\epsilon_i+\Omega_i)=\sum_{|\vec{k}\rangle}\sum_{|\lambda\rangle}\frac{|\vec{k}\rangle|\lambda\rangle\langle\lambda|\langle\vec{k}|}{\epsilon_i+\Omega_i-\epsilon(\vec{k})-\Omega_\lambda}\approx g_0(\epsilon_i)$$

and τ becomes

$$\tau(\epsilon_i+\Omega_i)\approx U(\vec{r},\{\vec{R}\})+U(\vec{r},\{\vec{R}\})g_0(\epsilon_i)U(\vec{r},\{\vec{R}\})+\cdots, \tag{6}$$

which is the transition operator for the problem of the electron scattered by the lattice with their atoms *fixed* at positions $\{\vec{R}\}$. Then, we can write

$$\mathscr{R}=\frac{1}{\hbar^2}\int_{-\infty}^{\infty}dt\ e^{i\omega t}\langle\langle a_{if}^*(\{\vec{R}\})a_{if}(\{\vec{R}\};t)\rangle\rangle, \tag{7}$$

where

$$a_{if}(\{\vec{R}\})=\langle\vec{k}_f|U(\vec{r},\{\vec{R}\})+U(\vec{r},\{\vec{R}\})g_0(\epsilon_i) \times U(\vec{r},\{\vec{R}\})+\cdots|\vec{k}_i\rangle \tag{8}$$

is the elastic scattering amplitude calculated for the *rigid* lattice, and

$$a_{if}(\{\vec{R}\};t)=e^{iH_{\rm ph}t/\hbar}a_{if}(\{\vec{R}\})e^{-iH_{\rm ph}t/\hbar}.$$

Therefore, the adiabatic approximation leads, as usual, to a separation of the electron and atomic motions.[18]

(ii) We will write $U(\vec{r},\{\vec{R}\})$ as a superposition of muffin-tin potentials centered on each atom:

$$U(\vec{r},\{\vec{R}\})=\sum_n U_{\rm mt}(|\vec{r}-\vec{R}_n|).$$

Then, reordering the right-hand side of Eq. (8), one can write $a_{if}(\{\vec{R}\})$ as a sum of amplitudes of scattering waves emanating from the atomic sites:[15,16]

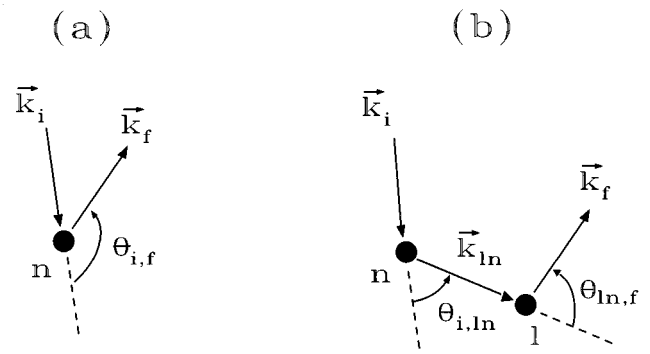

FIG. 1. Schematic representation of the electron paths corresponding to (a) a single-scattering (SS) wave and (b) a double-scattering (DS) wave.

$$a_{if}(\{\vec{R}\})=\sum_n a_n+\sum_n \sum_{l\neq n} a_{nl}+\cdots, \tag{9}$$

where a_n is the amplitude of the single-scattering (SS) wave emanating from the atom at $\vec{R}_n$, a_{nl} is the amplitude of the double-scattering (DS) wave product of the scattering at $\vec{R}_l$ of the SS wave emanating from $\vec{R}_n$, and so on. A schematic representation of the electron paths corresponding to SS and DS waves is shown in Figs. 1(a) and 1(b), respectively. Using the ''plane-wave'' approximation for the multiple scattering waves, a_n and a_{nl} can be written as[16]

$$a_n=\frac{2\pi}{V}\frac{\hbar^2}{m}f(\theta_{i,f})e^{-i\vec{k}\cdot\vec{R}_n}e^{-L_n/2\lambda} \tag{10}$$

and

$$a_{nl}=\frac{2\pi}{V}\frac{\hbar^2}{m}f(\theta_{i,ln})e^{-i\vec{k}_1\cdot\vec{R}_n}\frac{1}{R_{nl}}f(\theta_{ln,f})e^{-i\vec{k}_2\cdot\vec{R}_l}e^{-L_{nl}/2\lambda}, \tag{11}$$

where $f(\theta)$ is the elastic scattering amplitude calculated for the potential $U_{\rm mt}(r)$, $\vec{k}$, $\vec{k}_1$, and $\vec{k}_2$ are the wave-vector changes at each collision: $\vec{k}=\vec{k}_f-\vec{k}_i$, $\vec{k}_1=\vec{k}_{ln}-\vec{k}_i$, and $\vec{k}_2=\vec{k}_f-\vec{k}_{ln}$, with $\vec{k}_{ln}=k_i\hat{R}_{ln}$ ($\vec{R}_{ln}=\vec{R}_l-\vec{R}_n$), $\theta_{i,f}$, $\theta_{i,ln}$, and $\theta_{ln,f}$ are the corresponding scattering angles (see Fig. 1), and where we have introduced the effect of the inelastic collisions with the crystal electrons by weighting each amplitude with an attenuation factor $e^{-L/2\lambda}$, where L is the total electron path inside the solid and λ is the electron mean free path.

(iii) We will keep the displacements of the atoms from the equilibrium positions, $\vec{u}_n=\vec{R}_n-\vec{R}_n^0$, only in the phase factors of the amplitudes. Then,

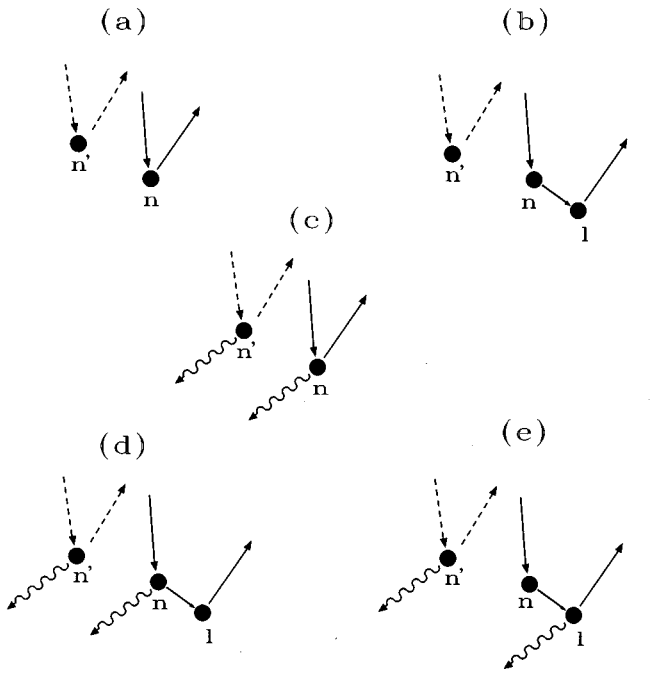

FIG. 2. Schematic representation of the interferences that give rise to the terms $\mathscr{R}^{(0)}$ and $\mathscr{R}^{(1)+}$: (a) interference between two SS waves, (b) interference between a SS wave and a DS wave, (c) interference between two one-phonon inelastic SS waves, (d) and (e) interferences between a one-phonon inelastic SS wave and one-phonon inelastic DS waves with excitation of the phonon at the first and at the second scatterer, respectively.

$$\mathscr{R}=\frac{1}{\hbar^2}\int_{-\infty}^{\infty}dt\ e^{i\omega t}\Bigg\{\sum_{n',n}a_{n'}^*a_n\langle\langle e^{i\vec{k}\cdot\vec{u}_{n'}}e^{-i\vec{k}\cdot\vec{u}_n(t)}\rangle\rangle + 2\,\mathrm{Re}\sum_{n',n}\sum_{l\neq n}a_{n'}^*a_{nl} \times\langle\langle e^{i\vec{k}\cdot\vec{u}_{n'}}e^{-i\vec{k}_1\cdot\vec{u}_n(t)}e^{-i\vec{k}_2\cdot\vec{u}_l(t)}\rangle\rangle+\cdots\Bigg\}, \tag{12}$$

where a_n and a_{nl} are now evaluated at the equilibrium positions $\{\vec{R}^0\}$.

(iv) *Harmonic* approximation. We will consider that the lattice vibrations can be treated within the harmonic approximation; then, we can use the Glauber formula:[19] $\langle\langle e^{iA}\rangle\rangle=e^{-1/2\langle\langle A^2\rangle\rangle}$, and Eq. (12) becomes

$$\mathscr{R}=\frac{1}{\hbar^2}\int_{-\infty}^{\infty}dt\ e^{i\omega t}\Bigg\{\sum_{n',n}a_{n'}^*a_n e^{-W_{n'}(\vec{k})}e^{-W_n(\vec{k})}e^{\langle\langle(\vec{k}\cdot\vec{u}_{n'})[\vec{k}\cdot\vec{u}_n(t)]\rangle\rangle}+2\,\mathrm{Re}\sum_{n',n}\sum_{l\neq n}a_{n'}^*a_{nl}e^{-W_{n'}(\vec{k})}e^{-W_n(\vec{k}_1)}e^{-W_l(\vec{k}_2)} \times e^{-\langle\langle(\vec{k}_1\cdot\vec{u}_n)(\vec{k}_2\cdot\vec{u}_l)\rangle\rangle}e^{\langle\langle(\vec{k}\cdot\vec{u}_{n'})[\vec{k}_1\cdot\vec{u}_n(t)]+(\vec{k}\cdot\vec{u}_{n'})[\vec{k}_2\cdot\vec{u}_l(t)]\rangle\rangle}+\cdots\Bigg\}, \tag{13}$$

where

$$W_n(\vec{k}) = \frac{1}{2}\langle\langle(\vec{k}\cdot\vec{u}_n)^2\rangle\rangle.$$

Equation (13) is our final expression for $\mathscr{R}$. It gives the transition rate from $|\vec{k}_i\rangle$ to $|\vec{k}_f\rangle$ in terms of the inelastic energy $\hbar\omega$, the electron elastic scattering amplitudes (calculated for the crystal with the atoms fixed at the equilibrium positions), and the time-dependent correlation functions $\langle\langle(\vec{k}_A\cdot\vec{u}_n)\cdot[\vec{k}_B\cdot\vec{u}_l(t)]\rangle\rangle$.

Our objective is to integrate Eq. (13) over ω to obtain the differential cross section $d\sigma/d\Omega$, which is the quantity really measured in the experiments of interest here. However, before performing this integration, in the next section we will extract the zero- and one-phonon contributions to $\mathscr{R}$.

B. Phonon expansion

The so-called phonon expansion of Eq. (13) consists in replacing the exponentials of the time-dependent correlation functions by their Taylor expansions:[14,17]

$$e^{\langle\langle(\vec{k}_A\cdot\vec{u}_n)[\vec{k}_B\cdot\vec{u}_l(t)]\rangle\rangle} = \sum_{m=0}^{\infty}\frac{\langle\langle(\vec{k}_A\cdot\vec{u}_n)[\vec{k}_B\cdot\vec{u}_l(t)]\rangle\rangle^m}{m!}. \tag{14}$$

The $m=0$ terms of these expansions give rise to the zero-phonon or elastic contribution to $\mathscr{R}$:

$$\mathscr{R}^{(0)} = \frac{2\pi}{\hbar^2}\delta(\omega)\left\{\sum_{n',n} a^*_{n'}a_n e^{-W_{n'}(\vec{k})}e^{-W_n(\vec{k})} + 2\,\mathrm{Re}\sum_{n',n}\sum_{l\neq n} a^*_{n'}a_{nl}e^{-W_{n'}(\vec{k})}e^{-W_n(\vec{k}_1)}e^{-W_l(\vec{k}_2)} \times e^{-\langle\langle(\vec{k}_1\cdot\vec{u}_n)(\vec{k}_2\cdot\vec{u}_l)\rangle\rangle} + \cdots\right\}. \tag{15}$$

The first term on the right-hand side of Eq. (15) corresponds to the interferences between SS waves and the second term to the interferences between SS and DS waves. Both type of interferences are shown schematically in Figs. 2(a) and 2(b). To exploit the two-dimensional symmetry of the problem, each sum over the atomic positions can be separated into a sum over the atoms in a layer and a sum over layers; the sums over the atoms in a layer can be performed analytically and give rise to the conservation law for the electron wave vector parallel to the surface: $\vec{k}_{f\|}=\vec{k}_{i\|}-\vec{g}_{hk}$, where $\vec{g}_{hk}$ is a vector of the reciprocal lattice of the surface. Therefore, the electrons scattered elastically are reflected only along a discrete set of directions, usually called Bragg directions.

The $m=1$ terms of the Taylor expansions give rise to the one-phonon contributions to $\mathscr{R}$. In the Appendix we show that these contributions can be written as

$$\mathscr{R}^{(1)\pm}(\vec{q}_\|,\alpha) = \frac{2\pi}{\hbar^2}\delta(\omega\pm\omega_\alpha(\vec{q}_\|))\left\{\sum_{n',n} a^*_{n'}a_n e^{-W_{n'}(\vec{k})}e^{-W_n(\vec{k})}\mathscr{A}^{\pm}_{n'}(\vec{q}_\|,\alpha;\vec{k})^*\mathscr{A}^{\pm}_{n}(\vec{q}_\|,\alpha;\vec{k}) + 2\,\mathrm{Re}\sum_{n',n}\sum_{l\neq n} a^*_{n'}a_{nl}e^{-W_{n'}(\vec{k})} \times e^{-W_n(\vec{k}_1)}e^{-W_l(\vec{k}_2)}e^{-\langle\langle(\vec{k}_1\cdot\vec{u}_n)(\vec{k}_2\cdot\vec{u}_l)\rangle\rangle}\mathscr{A}^{\pm}_{n'}(\vec{q}_\|,\alpha;\vec{k})^*[\mathscr{A}^{\pm}_{n}(\vec{q}_\|,\alpha;\vec{k}_1)+\mathscr{A}^{\pm}_{l}(\vec{q}_\|,\alpha;\vec{k}_2)] + \cdots\right\}, \tag{16}$$

where the plus and minus signs correspond to the transition rates for the electron scattering with *excitation* and *absorption*, respectively, of a phonon of wave vector parallel to the surface $\vec{q}_\|$, quantum number α, and frequency $\omega_\alpha(\vec{q}_\|)$. The functions $\mathscr{A}^{\pm}_n(\vec{q}_\|,\alpha;\vec{k})$ are defined in the Appendix. Note that the products $e^{-W_n(\vec{k})}\mathscr{A}^{\pm}_n(\vec{q}_\|,\alpha;\vec{k})$ and $e^{-W_n(\vec{k}_1)}e^{-W_l(\vec{k}_2)}e^{-\langle\langle(\vec{k}_1\cdot\vec{u}_n)(\vec{k}_2\cdot\vec{u}_l)\rangle\rangle}[\mathscr{A}^{\pm}_n(\vec{q}_\|,\alpha;\vec{k}_1)+\mathscr{A}^{\pm}_l(\vec{q}_\|,\alpha;\vec{k}_2)]$ are the probability amplitudes of exciting or absorbing a phonon $(\vec{q}_\|,\alpha)$ associated to the SS and DS electron paths of Figs. 1(a) and 1(b), respectively.

Figures 2(c)–2(e) show schematically the interferences that give rise to the three terms of Eq. (16). Again, as in the elastic scattering, the sums over the atoms in one layer in Eq. (16) give rise to a conservation law for the electron wave vector parallel to the surface: $\vec{k}_{f\|}=\vec{k}_{i\|}-\vec{g}_{hk}\mp\vec{q}_\|$. Thus, the electrons scattered having excited or absorbed a phonon $(\vec{q}_\|,\alpha)$ are also reflected only along a discrete set of directions.

In general, if one or several phonons are excited or absorbed during the scattering, the electron will be reflected in a discrete set of directions with $\vec{k}_{f\|}=\vec{k}_{i\|}-\vec{g}_{hk}-\Sigma_\nu\sigma_\nu\vec{q}^{(\nu)}_\|$, where $\sigma_\nu=+1$ if a phonon of wave vector $\vec{q}^{(\nu)}_\|$ is excited and $\sigma_\nu=-1$ if it is absorbed. These Bragg laws for the electron wave vector parallel to the surface follow from the conservation of the *total* wave vector parallel to the surface, which is a direct consequence of the discrete translational symmetry of the problem.

Therefore, the inelastic scattering is a totally *coherent* process, and the XPD/AED character of the MEED pattern cannot be assigned to a ''loss of coherence'' due to an inelastic event, as assumed in previous works. In the next sections we shall analyze which is the origin of the XPD/AED-like behavior.

C. The observed intensity

In a typical LEED or MEED experiment the electrons scattered *elastically* are not separated from those scattered *inelastically* by excitation and/or absorption of phonons. This is so because the phonon energies are much smaller than the typical energy resolutions in the experiments ($\sim$1 eV).

Therefore, the intensity measured in a LEED or MEED experiment is the sum of the *elastic* intensity plus the intensities of all the *inelastic* events. In our formulation this intensity is obtained by integrating $d^2\sigma/d\Omega d\epsilon$ over all the inelastic energies $\hbar\omega$. Since $e^{i\omega t}$ is the only ω dependence in Eq. (13), the integration over ω gives a $\delta(t)$ term and the integration over t gives

$$\frac{d\sigma}{d\Omega}=V^2\frac{m^2}{4\pi^2\hbar^4}\frac{k_f}{k_{iz}}\left\{\sum_{n',n}a_{n'}^{*}a_n e^{-W_{n'}(\vec{k})}e^{-W_n(\vec{k})}e^{\langle\langle(\vec{k}\cdot\vec{u}_{n'})(\vec{k}\cdot\vec{u}_n)\rangle\rangle}\right.$$
$$\left.+2\,\mathrm{Re}\sum_{n',n}\sum_{l\neq n}a_{n'}^{*}a_{nl}e^{-W_{n'}(\vec{k})}e^{-W_n(\vec{k}_1)}e^{-W_l(\vec{k}_2)}e^{-\langle\langle(\vec{k}_1\cdot\vec{u}_n)(\vec{k}_2\cdot\vec{u}_l)\rangle\rangle}e^{\langle\langle(\vec{k}\cdot\vec{u}_{n'})(\vec{k}_1\cdot\vec{u}_n)+(\vec{k}\cdot\vec{u}_{n'})(\vec{k}_2\cdot\vec{u}_l)\rangle\rangle}+\cdots\right\}. \quad (17)$$

This cross section is the quantity to be compared with the intensities measured in the experiments. We will show in the next section that the intensity calculated with Eq. (17) presents the two regimes observed experimentally: the LEED-like regime at low energies and the XPD/AED-like regime at medium energies.

A mathematical explanation of the occurrence of these two types of intensity patterns is as follows. In the limit of low energies all the exponentials in Eq. (17) can be approximated by one and the intensity becomes the intensity of an electron scattered from a lattice with the atoms fixed at the equilibrium positions. In the other limit, at high energies, the products of exponentials in Eq. (17) go to zero except when $n'=n$ or $n'=l$. The three "special" cases which originate in making $n'=n$ and $n'=l$ are shown schematically in Fig. 3. The sum over n of the interferences depicted in Fig. 3(a) produces only a smooth background. It is the sum of the interferences shown in Fig. 3(b) that produce the XPD/AED-like intensity pattern; in effect, the two waves of Fig. 3(b) share the same path to the first scatterer and therefore can accumulate a phase difference only in the *exit* path. On the contrary, the waves depicted in Fig. 3(c) can accumulate a phase difference only in the *incoming* path; therefore, the sum of these interferences should account for what has been called the "diffraction of the incident beam."[8,13]

A more physical explanation of the two regimes of the total intensity can be obtained by thinking in terms of phonons excited and/or absorbed during the scattering. To this purpose we will separate the contributions to Eq. (17) of the electrons scattered elastically and that of *all* the electrons scattered having excited or absorbed one phonon. The elastic or zero-phonon contribution is obtained readily integrating Eq. (4) with $\mathscr{R}=\mathscr{R}^{(0)}$. The one-phonon contribution can be obtained by either summing Eq. (16) over all the phonon modes or replacing in Eq. (13) the time-dependent exponential functions by their arguments and then performing the integrations over ω and t; in any case one obtains

$$\frac{d\sigma}{d\Omega}^{(1)}=V^2\frac{m^2}{4\pi^2\hbar^4}\frac{k_f}{k_{iz}}\left\{\sum_{n',n}a_{n'}^{*}a_n e^{-W_{n'}(\vec{k})}e^{-W_n(\vec{k})}\langle\langle(\vec{k}\cdot\vec{u}_{n'})(\vec{k}\cdot\vec{u}_n)\rangle\rangle+2\,\mathrm{Re}\sum_{n',n}\sum_{l\neq n}a_{n'}^{*}a_{nl}e^{-W_{n'}(\vec{k})}e^{-W_n(\vec{k}_1)}\right.$$
$$\left.\times e^{-W_l(\vec{k}_2)}e^{-\langle\langle(\vec{k}_1\cdot\vec{u}_n)(\vec{k}_2\cdot\vec{u}_l)\rangle\rangle}\langle\langle(\vec{k}\cdot\vec{u}_{n'})(\vec{k}_1\cdot\vec{u}_n)+(\vec{k}\cdot\vec{u}_{n'})(\vec{k}_2\cdot\vec{u}_l)\rangle\rangle+\cdots\right\}. \quad (18)$$

Equations (15), (17), and (18) will be used in the next section to analyze the transition of the intensity pattern from LEED-like at low energies to XPD/AED-like at medium energies.

Finally, to compare with the experimental results one must define the correlation functions $\langle\langle(\vec{k}_A\cdot\vec{u}_n)\cdot(\vec{k}_B\cdot\vec{u}_l)\rangle\rangle$, which in turn requires the formulation of a model for the lattice vibrations. We will adopt a Debye model, $\omega=cq$, for which the correlation functions can be written as[20,21]

$$\langle\langle(\vec{k}_A\cdot\vec{u}_n)\cdot(\vec{k}_B\cdot\vec{u}_l)\rangle\rangle=(\vec{k}_A\cdot\vec{k}_B)\sigma^2(\theta)F(x,\theta), \quad (19)$$

where $\sigma^2(\theta)$, the mean-square amplitude of vibration of the atoms, is

$$\sigma^2(\theta)=\frac{3\hbar^2}{4Mk_B\theta_D}\left[1+4\theta^2\int_0^{1/\theta}\frac{z\,dz}{e^z-1}\right],$$

with $\theta=T/\theta_D$, and where the function $F(x,\theta)$, with $x=q_D|\vec{R}_n-\vec{R}_l|$, is almost independent of θ and falls rapidly to zero when x increases (θ_D and q_D are the Debye temperature and wave vector, respectively). In Fig. 4 we have plotted $F(x,\theta)$ for $\theta=1.042$.

III. RESULTS

In this section we will compare intensity patterns calculated using the model presented in the previous section with

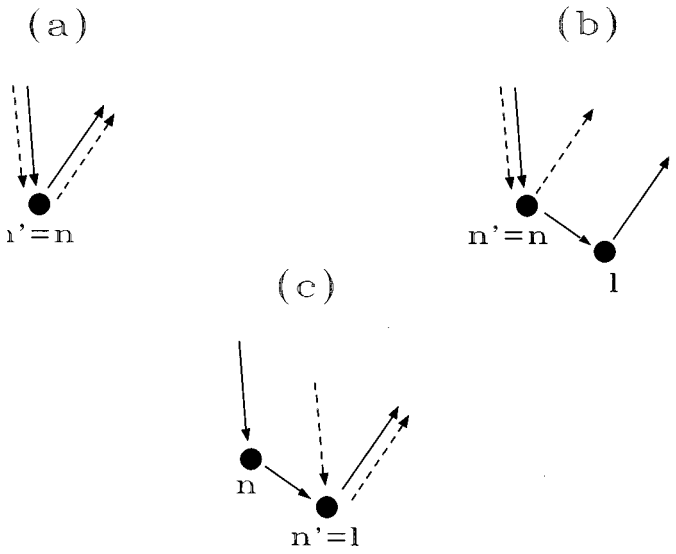

FIG. 3. Schematic representation of the three "special" types of interferences that occur when one makes $n'=n$ and $n'=l$ in Eq. (17). (a) Interference between two SS waves with $n'=n$, (b) interference between a SS wave and a DS wave with $n'=n$, and (c) interference between a SS wave and a DS wave with $n'=l$.

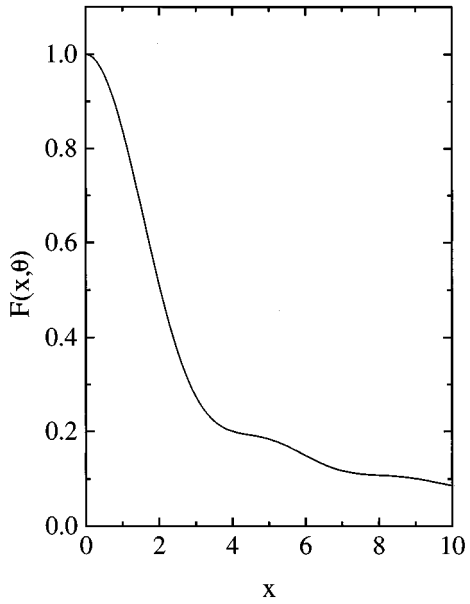

FIG. 4. Correlation function $F(x,\theta)$ defined in Eq. (19) calculated for $\theta=1.042$ and $q_D=1.71$ Å^{-1}.

intensity patterns measured on Cu(001) in the energy range 200–1500 eV.

The calculated intensity patterns are presented decomposed into the zero-, one-, and multiphonon contributions, where this latter is the difference between the total intensity [Eq. (17)] and the zero- plus one-phonon contributions. We have used $f(\theta)$ computed by the standard partial-wave method using the muffin-tin potential of Ref. 22, $\lambda=0.39$ Å $(E/eV)^{1/2}$,[23] and $\theta_D=283°$ K, i.e., slightly lower than the bulk value (315° K) to account for the larger displacements of the atoms at the surface. The refraction of the electron at the surface was also included by considering an inner potential of 14.1 eV.[23] For the one- and multiphonon contributions we considered up to the interferences between DS waves, whereas for the elastic contribution we included also the interferences between SS and triple-scattering waves. The sums over atoms were evaluated in the following way: (i) for the sums over second and third scatterers we considered all the atoms within a distance of 2.5 lattice constants of the previous scatterer, and (ii) for the double sums over atoms belonging to different electron paths but connected by a correlation function we considered all the atoms separated by a distance equal to or less than a lattice constant. Finally, to compare with the experiments, we have integrated the intensities over the cones defined by the angular acceptances of the analyzers; the integration of the elastic contribution was made analytically assuming a δ-like angular dependence, and that of the one- and multiphonon contributions were made numerically using a nine-point grid.

The experimental results are in the form of polar intensity plots (PIP's) along the [100] azimuth taken with two different geometries as shown in Fig. 5: (a) constant scattering angle during the scan and (b) constant incident direction.

Figure 6 presents results obtained in our laboratory with the constant scattering-angle geometry. The angular resolution was estimated to be $\pm 5°$ and the intensities have been normalized to the intensities measured under the same conditions in polycrystalline Cu. In the PIP's of 200 and 400 eV the arrows indicate the polar angles at which Bragg directions enter into the analyzer, whereas in the PIP of 800 eV they indicate the polar angles at which the main crystallographic directions enter into the analyzer. The three PIP's illustrate nicely the transition from a LEED-like intensity pattern at low energies to a XPD/AED-like intensity pattern at medium energies. The PIP of 200 eV is dominated by LEED effects. The two main peaks correspond to the (20) and (11) diffracted beams and the small peak at 26° to the (02) diffracted beam; the (1 3) diffracted beam is lost in the background. At 400 eV the LEED peaks still dominate the PIP, but they are less intense than at 200 eV. There is a rising background and a prominent structure at 45° that is not associated to any Bragg direction. Finally, at 800 eV all the LEED peaks have disappeared completely, leaving a PIP similar to those observed in XPD and AED experiments: two broad peaks at 0 and 45°, which correspond to exit directions along the internuclear axes [001] and [101], respectively, and a smaller structure at $\sim 20°$.

Figure 7 presents the PIP's calculated for the constant-scattering angle geometry [Fig. 5(a)]. To simulate the experimental normalization to polycrystalline Cu we have normalized the calculated intensity to the $T=\infty$ limit of Eq. (17). It is seen in the figure that all the main features of the experimental PIP's are well reproduced by the calculation, particularly the transition from one regime to the other at 400 eV. The PIP at 200 eV is dominated by the peaks corresponding to the (20) and (11) diffracted beams. At 400 eV the LEED peaks still dominate the PIP but with a lower intensity; an important increase of the background and a broad structure at $45°-50°$ are also observed. Finally, at 800 eV the PIP contains only two broad peaks at 0 and 45° and a smaller structure at $\sim 20°$.

There are some minor discrepancies with the PIP's of Fig. 6 that in general can be ascribed to our use of only DS waves (and of triple-scattering waves in the zero-phonon contribu-

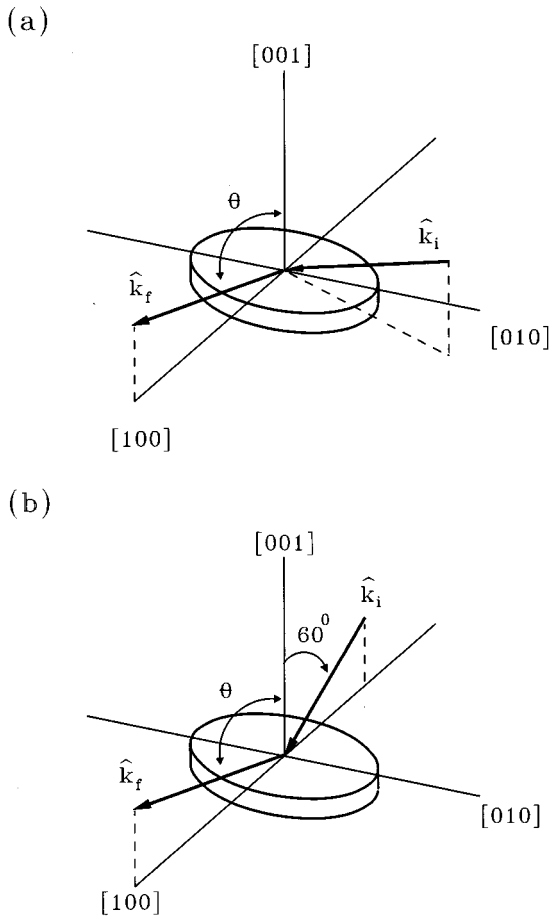

FIG. 5. (a) Constant scattering-angle geometry of Ref. 16; the polar and azimuthal angles of the incident beam vary during the scan as: $\cos\theta_i = 0.7071\cos(\theta+15°) + 0.5\sin(\theta+15°)$ and $\cos\Phi_i^{[100]} = [0.7071\sin(\theta+15°) - 0.5\cos(\theta+15°)]/\sin\theta_i$; the scattering angle remains fixed at $\theta_{i,f} = 144.35°$. (b) Constant incident-direction geometry of Ref. 13; the electron impinges along the [100] azimuth at 60° from the surface normal; the scattering angle varies during the scan as $\theta_{i,f} = 120° - \theta$.

tion) to treat the multiple scattering. For example, to reduce the relative intensity of the peak at 45° in the PIP of 800 eV one needs to include the so-called *defocusing* effect, what is accomplished by including higher-order scattering waves in the calculation.[9,24] The prediction of a single structure between 45° and 50° in the PIP of 400 eV, instead of a broad peak at 45° and the $(\bar{2}\ 5)$ LEED peak at 52° observed in Fig. 6, is ascribed to the combined effect of having overestimated the multiphonon contribution at 45° (as at 800 eV) and having underestimated the zero- and one-phonon contributions. Again, the inclusion of higher-order scattering waves in the calculation is expected to improve the agreement with the experimental PIP.

Figure 8 presents results obtained by Gao and Park with a constant incident-direction geometry [Fig. 5(b)]. The meaning of the arrows is the same as in Fig. 6. The PIP at 600 eV is dominated by the peaks corresponding to the $(1\ \bar{1})$ and (00) diffracted beams; minor structures are observed close to the $(3\ \bar{3})$ and $(2\ \bar{2})$ Bragg directions, between 40° and 50°, and at ~ 70° and 80°. In the PIP at 1500 eV the region

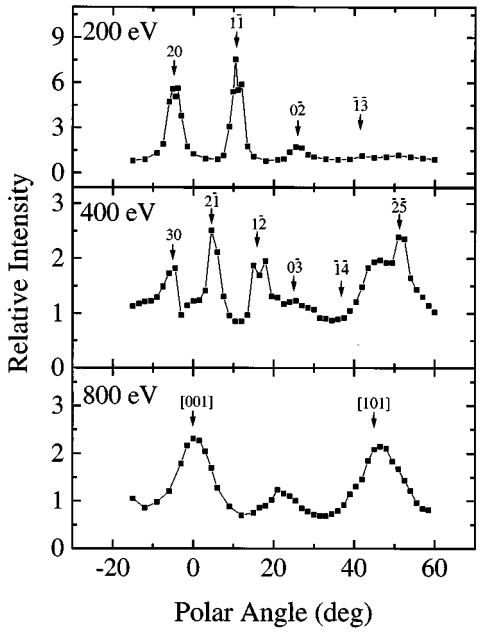

FIG. 6. Polar intensity plots obtained with the constant scattering-angle geometry of Fig. 5(a). The meaning of the arrows is explained in the text.

between −10° and 50° is similar to that of the PIP at 800 eV in Fig. 6, with two major peaks at 0° and 45° and a smaller structure at ~20°. The region above 50° is dominated by a large peak at 69° with two side peaks at 59° and 79°. It is seen that the peaks at 45°, 59°, and 79° may have contributions from the $(1\ \bar{1})$, (00), and (11) diffracted beams.

The calculated PIP's for the geometry of Gao and Park are shown in Fig. 9. Except for the relative intensities of the

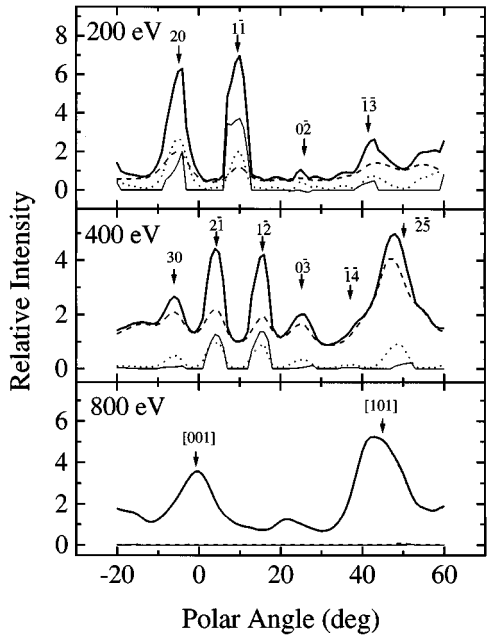

FIG. 7. Polar intensity plots calculated for the geometry of Fig. 5(a). The thin solid line corresponds to the elastic or zero-phonon term, the dotted line to the one-phonon term, and the broken line to the multiphonon term.

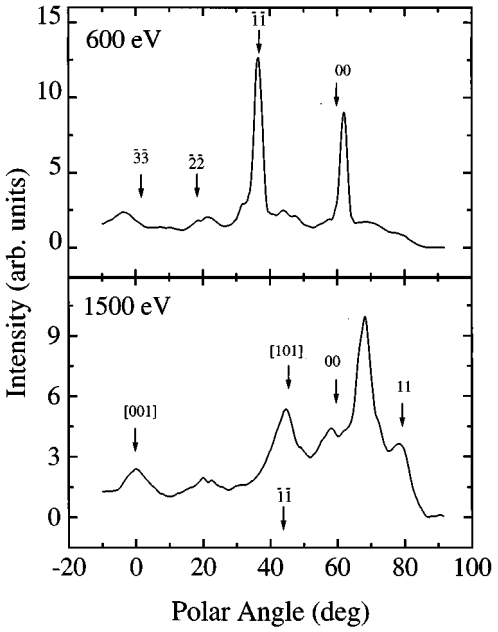

FIG. 8. Polar intensity plots obtained with the constant incident-direction geometry of Fig. 5(b) (taken from Ref. 13).

$(\bar{1}\,1)$ and (00) LEED peaks in the PIP of 600 eV, which are inverted, and for the region above 50° in the PIP of 1500 eV, the agreement between calculated and measured PIP's is again fairly good. Note that the two main LEED peaks in the experimental PIP of 600 eV (Fig. 8) have accompanying structures at lower angles that are reproduced by the calculation; the structure between 40° and 50° is also reproduced by the calculation, although not its double structure. All the other minor structures, near the $(\bar{3}\,3)$ and $(\bar{2}\,2)$ Bragg directions and at ~70° and 80°, are also present in the calculated PIP. At 1500 eV the calculated PIP reproduces correctly the relative intensities of the three peaks at 0, 20°, and 45°. In the region above 50° the calculation predicts correctly three peaks as observed in the experiment, but fails to reproduce their positions and the high intensity of the central peak. Note that the relative intensities of the two side peaks are correct. Therefore, the only major point of disagreement between the measured and calculated PIP's of 1500 eV is the high intensity of the peak observed at 69°. The cause of this disagreement is not clear yet.

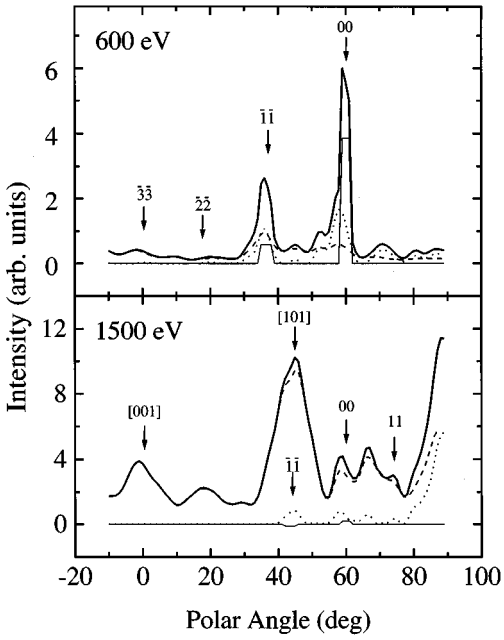

FIG. 9. Polar intensity plots calculated for the geometry of Fig. 5(b). The thin solid line corresponds to the elastic or zero-phonon term, the dotted line to the one-phonon term, and the broken line to the multiphonon term.

IV. DISCUSSION

Having demonstrated in the previous section that the model reproduces fairly well the main features of the experimental PIP's, in this section we will analyze the interplay of the different contributions to the total intensity. The aim will be to identify the nature of the transition from the LEED-like intensity pattern at low electron energies to the XPD/AED-like intensity pattern at medium energies.

We begin with the analysis of the three contributions in the PIP of 200 eV in Fig. 7. The elastic or zero-phonon contribution is different from zero only around the Bragg directions, as anticipated in our discussion in Sec. II B. The width of the peaks is essentially that of the acceptance cone of the analyzer, whereas the intensities, which vary from peak to peak, are determined by the interference between layers and by the Debye-Waller (DW) factors. However, as the DW factors depend on the energy and the scattering angle, which in this geometry are constant during the scan, the relative intensities in this case are determined solely by the interference between layers. This is the cause of the low intensities of the $(0\bar{2})$ and $(\bar{1}\,3)$ peaks. The one-phonon contribution also peaks at the Bragg directions, indicating that the excitation or absorption of phonons with $q \approx 0$ is the dominant process. This is the most important contribution to the peak $(\bar{2}0)$ and the second most important contribution to the peak $(\bar{1}1)$. The multiphonon contribution presents a smooth variation with small broad peaks at the Bragg directions; it is the dominant contribution outside these directions.

At 400 eV the zero-phonon contribution has the same characteristics as at 200 eV; the only important difference is the reduced intensity of the most important peaks. The one-phonon contribution is again centered around the Bragg directions, being negligible outside these directions; this contribution is now as important as or more important than the zero-phonon contribution. The multiphonon contribution is again responsible for all the background in the PIP and has well-defined peaks at all the Bragg directions. We think that these peaks are likely produced by the two-phonon and eventually the three-phonon contributions, which are expected to dominate the multiphonon contribution at this energy, and which, like the one-phonon contribution, may still be centered around the Bragg directions.

Finally, at 800 eV, when the PIP has reached its XPD/AED-like final form, the zero- and one-phonon contributions are completely negligible and the PIP is due almost entirely to the multiphonon contribution.

In the PIP's of Fig. 9 the scattering angle varies during the scan and therefore the DW factors also intervene in determining the relative intensities of the peaks. In fact, they are the main cause of the vanishing intensities of the (3 3) and (2 2) LEED peaks in the PIP of 600 eV. The zero-phonon contribution in this PIP is different from zero only at the (1 1) and (00) Bragg directions. The one-phonon component also contributes to the (1 1) and (00) peaks and is the main responsible for the structures of these peaks at lower angles and for the small peaks at 70 and 80°. The multiphonon contribution accounts for all the background and has a small peak at the (1 1) Bragg direction and a steplike change at the (00) Bragg direction.

At 1500 eV the zero-phonon contribution has disappeared almost completely and only a residual one-phonon contribution remains near the (1 1), (00), and (11) Bragg directions, and at ~66°. The multiphonon contribution accounts for all the intensity below 40° and is the largest contribution in the rest of the PIP.

Therefore, the analysis of the different contributions to the total intensity shows that the LEED-like and the XPD/AED-like intensity patterns correspond to the limiting cases of completely elastic scattering and of inelastic scattering with excitation/absorption of multiple phonons.

It is important to note that although at medium energies the multiphonon contribution behaves as the intensity in XPD and AED experiments, *none* of the inelastic scattering events contributing to it has an XPD/AED-like intensity pattern. It was shown in Sec. II B that any inelastic scattering event is a totally coherent process and that the electrons emerge from the surface along a discrete set of directions determined by the conservation of the *total* wave vector parallel to the surface. It is the *sum* of the intensities of all the inelastic diffracted beams that produces the XPD/AED-like intensity pattern.

We have also found that the LEED-like intensity pattern survives the excitation or absorption of a low number of phonons. Therefore, at low energies the total intensity (like the elastic contribution) obeys a pseudoconservation of the electron wave vector parallel to the surface. This pseudoconservation rule relaxes gradually as the energy is increased and with it the mean number of phonons exchanged with the crystal.

A rough estimate of the number of phonons exchanged with the crystal can be obtained as follows: ignoring the multiple scattering of the electron, i.e., keeping only the first term in the right-hand side of Eq. (13), the probability of exchanging m phonons with the crystal is proportional to

$$P_m \propto e^{-1/2\langle\langle(\vec{k}\cdot\vec{u}_{n'})^2\rangle\rangle} e^{-1/2\,\langle\langle(\vec{k}\cdot\vec{u}_n)^2\rangle\rangle} \times \int_{-\infty}^{\infty} dt\; e^{i\omega t} \frac{\langle\langle(\vec{k}.\vec{u}_{n'})[\vec{k}.\vec{u}_n(t)]\rangle\rangle^m}{m!}, \qquad (20)$$

which according to Eq. (19) is roughly proportional to

$$P_m \propto e^{-k^2\sigma^2} \frac{(k^2\sigma^2)^m}{m!}. \qquad (21)$$

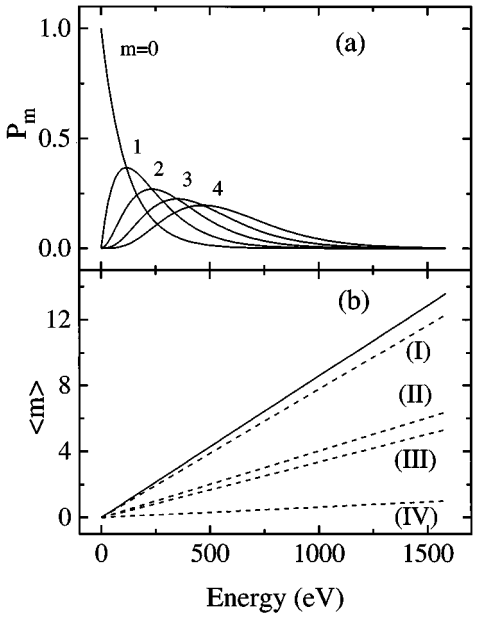

FIG. 10. (a) Probability of exchanging m phonons with the crystal calculated with Eq. (21) for the geometry of Fig. 5(a). (b) Mean number of phonons excited or absorbed during the scattering calculated for the constant scattering-angle (full line) and constant incident-direction geometries [broken line; (I): $\theta=-10°$; (II): $\theta=38.6°$; (III): $\theta=46.9°$; (IV): $\theta=90°$].

Thus, the probability of exchanging m phonons with the crystal is maximum at $k^2\approx m/\sigma^2$ and the mean number of phonons exchanged during the scattering is $\langle m\rangle\approx k^2\sigma^2$.

Then, the transition from the LEED regime to the MEED regime expressed in the three panels of Fig. 7 can now be reinterpreted with the aid of Fig. 10 as follows. When the mean number of phonons exchanged with the crystal is low, $\langle m\rangle=0-2$, a LEED-like intensity pattern is observed, when $\langle m\rangle=3-4$ both a LEED-like and a XPD/AED-like intensity patterns coexist, and when $\langle m\rangle$ exceeds 5–6 a XPD/AED-like intensity pattern is observed.

For the analysis of Fig. 9 in terms of the mean number of phonons exchanged with the crystal we have to take into account that $\langle m\rangle$ varies during the scan. Following the above criterion to determine the regions of dominance of each regime, in the PIP of 600 eV the region above 46.9° should be LEED-like, whereas in the PIP of 1500 eV the region below 38.6° should be XPD/AED-like, which is in complete agreement with the content of Fig. 8.

V. CONCLUSIONS

We have presented a treatment of the scattering of electrons from crystalline surfaces that allows one to calculate the zero-, one-, and multiphonon contributions to the intensity of the ''elastic'' peak as measured in LEED and MEED experiments.

The treatment is based on a separation of the electron and atomic motions (*adiabatic* approximation) and on a cluster-type formulation of the multiple scattering of the electron. The inelastic scattering events are treated as coherent processes and no break of the phase relation between the incident and the exit paths of the electron is assumed.

The LEED and the MEED regimes appear quite naturally in this model as the limit cases of completely elastic scattering and of inelastic scattering with excitation or absorption of multiple phonons, respectively. The transition from one regime to the other is explained as follows. At low electron energies the scattering with excitation or absorption of zero (elastic) or a low number of phonons dominate and a LEED-like intensity pattern is observed. As the energy is increased the probability of exciting and/or absorbing a larger number of phonons increases and XPD/AED-like features begin to develop and eventually dominate the intensity pattern.

It is important to note that in contrast to the LEED regime, in which to each scattering event corresponds an intensity pattern similar to the one observed, in the MEED regime *none* of the scattering events has an intensity pattern like the one observed. The XPD/AED-like intensity pattern characteristic of the MEED regime results from the sum of the intensities of many different inelastic scattering events, each of which has its own LEED-like intensity pattern determined by the conservation of the *total* wave vector parallel to the surface.

A calculation of the intensity of electrons scattered from Cu(001) at low and medium energies is in very good agreement with experimental results obtained using two different geometries. In particular, it reproduces correctly the transition between the two regimes in both cases.

We have found that the parameter $\langle m\rangle = k^2\sigma^2$, which we take as the mean number of phonons exchanged with the crystal during the scattering, can be used to define the regions of dominance of each regime. A LEED-like intensity pattern is observed for $\langle m\rangle \leqslant 2$, both LEED-like and XPD/AED-like features coexist for $\langle m\rangle \approx 3-4$, and finally a XPD/AED-like intensity pattern is observed when $\langle m\rangle \geqslant 5-6$. We have shown that in experiments in which $k^2\sigma^2$ varies during the scan one part of the PIP may be in one regime and the rest in another.

ACKNOWLEDGMENTS

We wish to acknowledge fruitful discussions with V.H. Ponce and R.O. Barrachina and the technical assistance of J. De Pellegrin and C. Wenger. Two of us (H.A. and G.Z.) are also members of the CONICET.

APPENDIX A: ONE-PHONON CONTRIBUTIONS TO $\mathscr{R}$

In this appendix we will derive an expression for the $m=1$ or one-phonon contributions to $\mathscr{R}$.

If we index each phonon mode with a wave vector parallel to the surface $\vec{q}_\parallel$ and a quantum number α, the time-dependent correlation functions can be written as[14]

$$\langle\langle(\vec{k}_A\cdot\vec{u}_{n'})[\vec{k}_B\cdot\vec{u}_n(t)]\rangle\rangle = \sum_{\vec{q}_\parallel,\alpha}\frac{\hbar}{2NM\omega_\alpha(\vec{q}_\parallel)}[\vec{k}_A\cdot\vec{\epsilon}_\alpha(\vec{q}_\parallel)][\vec{k}_B\cdot\vec{\epsilon}_\alpha(\vec{q}_\parallel)]e^{i\vec{q}_\parallel\cdot(\vec{R}^0_n-\vec{R}^0_{n'})} \times\{n_\alpha(-\vec{q}_\parallel)e^{i\omega_\alpha(\vec{q}_\parallel)t}+[n_\alpha(\vec{q}_\parallel)+1]e^{-i\omega_\alpha(\vec{q}_\parallel)t}\}, \tag{A1}$$

where N and M are the number of atoms in the crystal and the atomic mass, respectively, and where $\omega_\alpha(\vec{q}_\parallel)$, $\vec{\epsilon}_\alpha(\vec{q}_\parallel)$, and $n_\alpha(\vec{q}_\parallel)$ are the frequency, polarization vector, and mean occupation number of the phonon mode $(\vec{q}_\parallel,\alpha)$.

Then, using Eq. (A1) in the $m=1$ terms of the phonon expansion of Eq. (13) one obtains

$$\mathscr{R}^{(1)} = \sum_{\vec{q}_\parallel,\alpha}\{\mathscr{R}^{(1)+}(\vec{q}_\parallel,\alpha)+\mathscr{R}^{(1)-}(\vec{q}_\parallel,\alpha)\},$$

where

$$\mathscr{R}^{(1)\pm}(\vec{q}_\parallel,\alpha) = \frac{2\pi}{\hbar^2}\delta[\omega\pm\omega_\alpha(\vec{q}_\parallel)]\Bigg\{\sum_{n',n}a^*_{n'}a_n e^{-W_{n'}(\vec{k})}e^{-W_n(\vec{k})}\mathscr{A}^\pm_{n'}(\vec{q}_\parallel,\alpha;\vec{k})^*\mathscr{A}^\pm_n(\vec{q}_\parallel,\alpha;\vec{k}) + 2\,\mathrm{Re}\sum_{n',n}\sum_{l\neq n}a^*_{n'}a_{nl} \times e^{-W_{n'}(\vec{k})}e^{-W_n(\vec{k}_1)}e^{-W_l(\vec{k}_2)}e^{-\langle\langle(\vec{k}_1\cdot\vec{u}_n)(\vec{k}_2\cdot\vec{u}_l)\rangle\rangle}\mathscr{A}^\pm_{n'}(\vec{q}_\parallel,\alpha;\vec{k})^*[\mathscr{A}^\pm_n(\vec{q}_\parallel,\alpha;\vec{k}_1)+\mathscr{A}^\pm_l(\vec{q}_\parallel,\alpha;\vec{k}_2)]+\cdots\Bigg\}, \tag{A2}$$

with

$$\mathscr{A}^+_n(\vec{q}_\parallel,\alpha;\vec{k}) = \left[\frac{\hbar(n_\alpha(\vec{q}_\parallel)+1)}{2NM\omega_\alpha(\vec{q}_\parallel)}\right]^{1/2}[\vec{k}\cdot\vec{\epsilon}_\alpha(\vec{q}_\parallel)]e^{i\vec{q}_\parallel\cdot\vec{R}^0_n} \tag{A3}$$

and

$$\mathscr{A}^-_n(\vec{q}_\parallel,\alpha;\vec{k}) = \left[\frac{\hbar n_\alpha(\vec{q}_\parallel)}{2NM\omega_\alpha(\vec{q}_\parallel)}\right]^{1/2}[\vec{k}\cdot\vec{\epsilon}_\alpha(\vec{q}_\parallel)]e^{i\vec{q}_\parallel\cdot\vec{R}^0_n} \tag{A4}$$

*Present address: Instituto de Ciencias de Materiales, Serrano 144, Madrid, Spain.

[1] C.S. Fadley, in *Synchrotron Radiation Research: Advances in Surface Science*, edited by R.Z. Bachrach (Plenum, New York, 1990).

[2] W.F. Egelhoff, Crit. Rev. Solid State Mater. Sci. **16**, 213 (1990); in *Ultrathin Magnetic Structures I, An Introduction to Electronic, Magnetic, and Structural Properties*, edited by J.A.C. Bland and B. Heinrich (Springer-Verlag, Berlin, 1994), Chap. 5.

[3] S.A. Chambers, Surf. Sci. Rep. **16**, 261 (1992).

[4] G. Allié, E. Blanc, D. Dufayard, and R.M. Stern, Surf. Sci. **46**, 188 (1974).

[5] A. Mosser, Ch. Burggraf, S. Goldsztaub, and Y.H. Ohtsuki, Surf. Sci. **54**, 580 (1976).

[6] H. Hilferink, E. Lang, and K. Heinz, Surf. Sci. **93**, 398 (1980).

[7] M.V. Gomoyunova, I.I. Pronin, and I.A. Shmulevitch, Surf. Sci. **139**, 443 (1984).

[8] S.A. Chambers, I.M. Vitomirov, S.B. Anderson, and J.H. Weaver, Phys. Rev. **35**, 2490 (1987); S.A. Chambers, I.M. Vitomirov, and J.H. Weaver, Phys. Rev. **36**, 3007 (1987).

[9] M.-L. Xu and M.A. Van Hove, Surf. Sci. **207**, 215 (1989).

[10] H. Cronacher, K. Heinz, K. Müller, M.-L. Xu, and M.A. Van Hove, Surf. Sci. **209**, 387 (1989).

[11] G.R. Harp, D.K. Saldin, and B.P. Tonner, Phys. Rev. Lett. **65**, 1012 (1990).

[12] H. Ascolani, M.M. Guraya, and G. Zampieri, Phys. Rev. B **43**, 5135 (1991).

[13] Y. Gao and K.T. Park, Phys. Rev. B **46**, 1743 (1992).

[14] N.W. Ashcroft and N.D. Mermin, *Solid State Physics* (Saunders College, Philadelphia, 1976), Appendix N.

[15] J.J. Barton, M.-L. Xu, and M.A. Van Hove, Phys. Rev. B **37**, 10 475 (1988).

[16] H. Ascolani, R. Barrachina, M.M. Guraya, and G. Zampieri, Phys. Rev. B **46**, 4899 (1992).

[17] J.R. Manson, Phys. Rev. B **43**, 6924 (1991).

[18] S.Y. Tong, C.H. Li, and D.L. Mills, Phys. Rev. B **21**, 3057 (1980).

[19] N.D. Mermin, J. Math. Phys. **7**, 1038 (1966).

[20] G. Beni and P.M. Platzman, Phys. Rev. B **14**, 1514 (1976).

[21] M. Sagurton, E.L. Bullock, and C.S. Fadley, Surf. Sci. **182**, 287 (1987).

[22] V.L. Moruzzi, J.F. Janak, and A.R. Williams, *Calculated Electronic Properties of Metals* (Pergamon, New York, 1978).

[23] S. Kono, S.M. Goldberg, N.F.T. Hall, and C.S. Fadley, Phys. Rev. B **22**, 6085 (1980).

[24] W.F. Egelhoff, Phys. Rev. Lett. **59**, 559 (1987).